Research Article | Vol. 10, No. 8 / 1 August 2019 / Biomedical Optics Express 4207

Biomedical Optics EXPRESS

Analysis of low-scattering regions in optical coherence tomography: applications to neurography and lymphangiography

VALENTIN DEMIDOV,[1,*] LEV A. MATVEEV,[2] OLGA DEMIDOVA,[3] ALEXANDER L. MATVEYEV,[2] VLADIMIR Y. ZAITSEV,[2] COSTEL FLUERARU,[4] AND I. ALEX VITKIN[1,5,6]

[1]*Department of Medical Biophysics, University of Toronto, 101 College St., Toronto, M5G 1L7, Canada*
[2]*Institute of Applied Physics Russian Academy of Sciences, 46 Ulyanov Street, Nizhniy Novgorod, 603950, Russia*
[3]*Department of Arts and Science, Seneca College, 1750 Finch Avenue East, Toronto, M2J 2X5, Canada*
[4]*National Research Council Canada, Information Communication Technology, 1200 Montreal Rd, Ottawa, K1A0R6, Canada*
[5]*University Health Network, Princess Margaret Cancer Centre, 610 University Ave, Toronto, M5G 2C1, Canada*
[6]*University of Toronto, Department of Radiation Oncology, 150 College St, Toronto, M5S 3E2, Canada*
[*]*val.demidov@mail.utoronto.ca*

Abstract: Analysis of semi-transparent low scattering biological structures in optical coherence tomography (OCT) has been actively pursued in the context of lymphatic imaging, with most approaches relying on the relative absence of signal as a means of detection. Here we present an alternate methodology based on spatial speckle statistics, utilizing the similarity of a distribution of given voxel intensities to the power distribution function of pure noise, to visualize the low-scattering biological structures of interest. In a human tumor xenograft murine model, we show that these correspond to lymphatic vessels and nerves; extensive histopathologic validation studies are reported to unequivocally establish this correspondence. The emerging possibility of OCT lymphangiography and neurography is novel and potentially impactful (especially the latter), although further methodology refinement is needed to distinguish between the visualized lymphatics and nerves.

1. Introduction

The lymphatic system and its role in cancer growth and metastasis have received increasing attention [1–3], suggesting it as prognostic and targetable feature for local tumor control. However, despite its clinical relevance, our understanding of its development and function in tumors lags far behind that of the other circulatory system of blood vasculature, mostly due to the limitations of available imaging techniques.

Effective *in-vivo* detection of optically semitransparent lymphatic microvasculature has proven to be extremely challenging. For example, radioactive (lymphoscintigraphy), magneto-chromatic (magnetic resonance lymphography), fluorescent (indocyanine green (ICG) lymphography) dyes or microbubbles (ultrasound lymphography) [4–7] have been injected into the tissue at the particular anatomical site of interest to image the local draining lymphatic network, a rather limited clinical approach. In animal models, high resolution intravital ICG fluorescence microscopy is commonly used to visualize the lymphatic vessels and lymph nodes in greater detail, albeit within a limited depth range (up to 0.3-0.4 mm) [8].

These techniques have proven useful in some aspects of preclinical research or clinical applications. However, none are optimal, suffering from issues that include poor spatial

#364831 https://doi.org/10.1364/BOE.10.004207
Journal © 2019 Received 12 Apr 2019; revised 24 Jun 2019; accepted 17 Jul 2019; published 26 Jul 2019

Biomedical Optics EXPRESS

resolution, contrast agent injection procedures that impact subject comfort or alter physiology, and potential chemical or radiation toxicity. Therefore, efforts continue to develop new and improved methodologies for *in-vivo* imaging lymphatic vessels and lymph nodes, ideally without the need for contrast agent injection. One such emerging technology potentially suitable for high-resolution label-free detection of lymphatic networks is optical coherence tomography (OCT), a 3D imaging modality for visualizing subsurface tissue details at resolutions approaching microscopy and blood flow details at the microcirculation level to a depth of 1 - 3 mm [9]. Recent advances in OCT technology have introduced dye-free imaging of tumor microenvironment, angiogenesis, lymphangiogenesis, tissue viability and responses to vascular-targeted and cellular-targeted therapies [1,10].

In conventional OCT cross-sectional structural imaging, lymphatic vessels appear as transparent structures of elongated shape with negligible scattering intensity. During the last decade, several research groups have been developing and improving lymphangiography methods based on such negative contrast of OCT intensity images [1,11,12]. However, optical transparency of lymph and resulting low-scattering OCT signal at levels approaching the system noise floor present significant challenges for *in-vivo* lymphatic vasculature detection. The presence of OCT speckles further complicates the correct visualization of lymphatic vessels; as speckle may be larger in size than one imaging pixel (depending on the specifics of the OCT system), signal amplitudes from otherwise high-scattering tissue areas may reach noise level due to destructive interference within a particular speckle, thus appearing as an erroneous lymph region. Further, OCT's signal reduction with depth requires phantom-based measurements of attenuation coefficients specific for each particular OCT imager to be used with low-signal amplitude thresholding approaches [13]. Recent reports suggesting solutions to these challenges take into account lymphatic vessels form, speckle median value in the chosen regions of interest, speckle decorrelation time and absence of the in-depth signal loss [12,14]. All these solutions, while effective to some degree, require complex and computationally expensive procedures.

Another important semi-transparent biological structure of interest is a nerve [15–17]. Peripheral nerve fibers innervate tumors [18,19] and interact with cancer cells [20,21] altering the behavior of tumor angiogenesis and growth [22] and serving as a dissemination pathway for invasion with spread to distant sites [23,24]. In clinical practice, magnetic resonance (MR) imaging is sometimes used for the whole- or partial-body neurography, mostly in neurosurgery [25]. Recently, a high-resolution MR neurography of diffuse peripheral nerve lesions was adopted with application to tumors >5 cm in diameter [26], limiting its use in the clinic and in preclinical studies. OCT's contribution to nerve imaging has been mostly confined to ophthalmology, specifically to retinal nerve fiber layer segmentation and correlation of changes of its thickness with various eye diseases [27]. The retinal nerve fibers appear on ocular OCT as a bright layer of eye distinguishable from adjacent anatomical layers [28]. The structure of peripheral nerves comprises one or more fascicles of several thousand nerve fibers. Fascicles are bound together by epineurium tissue tens of microns thick [29]. Nerve fibers themselves are positively contrasted in the OCT images but electrically insulating tissues around them are semi-transparent [30]. To date, reports of OCT nerve imaging outside of ophthalmology have been limited to visualization of large (~1 mm in diameter) peripheral nerves in animal models following traumatic crush injury, suture ligation, and transection [31–33].

Here we propose a novel approach to OCT lymphangiography/neurography that addresses the negative contrast challenges by utilizing the statistical nature of OCT speckles [34]. Speckle statistics report on spatial and temporal distribution properties of OCT signal to be utilized for characterization of biological tissues [34–36]. Since as mentioned we are interested in detecting lymphatic and nerve low-signal regions that are hard to separate from noise, we quantify their similarities / differences using speckle statistics (rather than simply comparing signal intensity levels). As validated by histological studies, the low-scattering near-noise level signals from

Biomedical Optics EXPRESS

lymphatic vessels and connective tissues around nerves exhibit speckle statistics similar to the power distribution function of pure noise. By quantifying this similarity and selecting a suitable threshold range, we demonstrate accurate OCT mapping of these two important components of tumor microenvironment, although further methodology refinement is needed to distinguish between the visualized lymphatics and nerves.

2. Materials and methods

2.1. Optical coherence tomography system

A swept-source OCT system based on a quadrature interferometer to suppress the complex conjugate artifact [37,38] was used in this study (Fig. 1). Its light source (HS2000-HL, Santec, Japan) with 20 kHz rotating-polygon-based tunable filter and wavelength centered at 1320 nm, had a sweep range of 110 nm and an average output power of 10 mW. The axial and lateral resolutions in air were 8 and 15 μm, respectively. OCT optical power at the probe output was measured before each imaging session to be 5 mW, OCT probe imaging angle was set to 86° relative to horizontal, and imaging speed was fixed at 40 frames per second (with 80% scanning galvo duty cycle of the imaging probe).

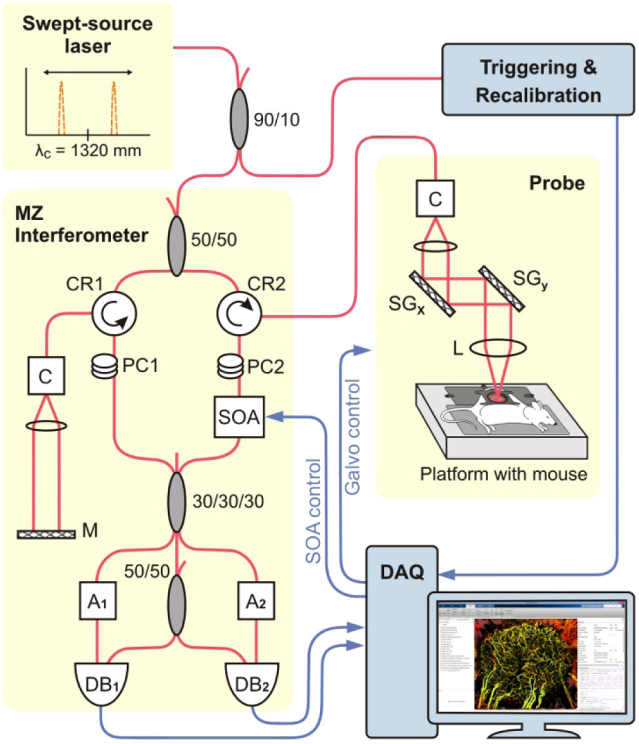

Fig. 1. Schematic diagram of the swept-source OCT system setup with quadrature Mach-Zehnder fiber-based interferometer and optical amplification: SOA - semiconductor optical amplifier, PC - polarization controller, A - fiber attenuator, DB - dual balanced photo-detector, DAQ - data acquisition card, C - collimator, MZ Interferometer - Mach-Zehnder interferometer, M - mirror. SG_x and SG_y - scanning mirrors driven by galvanometers in x and y lateral dimensions, CR - circulator, L - lens. Red lines represent optical paths, blue lines are electrical signals.

As schematically shown in Fig. 1, the amplified signal was combined with the reference signal in a 3 × 3 coupler followed by a 2 × 2 coupler for two channels balanced detection to extract the

Biomedical Optics EXPRESS

components of the complex interferometric signal. A 120° phase shift between each channel was recalculated into a 90° phase shift using trigonometric equations as previously described [37]. DC component of each channel's detector signal was subtracted prior to recording of the full complex spectral amplitude $S(n)$ for each of 2048 spectral bandwidth components n:

$$S(n) = Q_1(n) + i \cdot Q_2(n), \tag{1}$$

with $Q_1(n)$ and $Q_2(n)$ corresponding to real and imaginary parts of full analytical complex signal. Physically obtained full complex signal eliminated the need for digital frequency modulation of the signal by Hilbert transform, for example as commonly performed for in-phase-only OCT systems [39]. Although addition of the physical quadrature is not critically important for the proposed method, it increases the signal-to-noise ratio and in part addresses the destructive interference challenge discussed in the introduction that may cause a low-signal artefact in the absence of real tissue lymphatics / nerves: at least one of the two channels will likely retain the constructive interference of the resultant complex OCT signal.

2.2. Mouse and tumor models

All animal procedures were approved by the University Health Network Institutional Animal Care and Use Committee in Toronto, Canada (AUP #3256). 7-8 weeks immune-compromised mice (NRG strain, Jackson Labs, ME, USA) with dorsal skin window chamber (DSWC) were used for experiments. Tumors were generated by injection of 2.5×10^5 human-derived pancreatic cancer cells (BxPC-3 cell line, AntiCancer Inc., San Diego, CA, USA) prepared in 10 µL of 1:1 PBS:Matrigel (BD Biosciences, ON, Canada) solution into the dorsal skin using 30G needles. DSWC installation was performed 15-21 days post injection after the tumors reached 3-5 mm diameter using the procedure described previously [10]. A mouse with installed DSWC is shown in Fig. 2(a).

To help interpret and to support *in-vivo* observations, animals were sacrificed after OCT imaging and tissues were extensively examined by histology using three different biological stains. Mice were euthanized by anesthesia with ketamine/xylazine followed by cervical dislocation. Tumors and normal skin tissues were resected, fixed in 10% formalin and processed for histologic staining. Hematoxylin and Eosin (H&E) staining was used to view cellular morphology; lymphatic vessel endothelial hyaluronan receptor 1 (LYVE-1) was used to visualize lymphatic vessels; and cells were distinguished from connective tissues (including the epineurium surrounding nerve fascicles) with Masson's Trichrome (MT) staining. Slides were scanned by Aperio Scanner and evaluated using Aperio ImageScope software (Leica Biosystems, Concord, ON, Canada).

2.3. OCT imaging and speckle statistical analysis

Volumetric OCT images were obtained *in-vivo* using normal and tumor-bearing mice in a dorsal skin window chamber model (Figs. 2(a,b)). Speckle statistical data was collected by recording 24 B-scans at each lateral location with 800 A-scans along the fast lateral scan axis and 1600 cross sections in the slow axis direction. In order to obtain 24 B-scans at the frame rate of 40 frames / second with a 20kHz OCT system, each B-scan was split into two frames. Due to the galvo mirror duty cycle of 80%, only 400 of A-scans were acquired per frame from possible 500. Merging two frames together resulted in 800 A-scans in each B-scan. Scanned tissue volumes (6 mm x 6 mm laterally, x ~1.5 mm in depth) were divided into smaller analysis volumes of $5\times3\times3$ pixels in size (slow lateral x fast lateral x depth) over 24 repetitive scans, yielding 1080 pixels for statistical calculations.

Typical B-scan at the tumor-normal tissue boundary is shown in Fig. 2(c) (location labeled with the blue line in Fig. 2(b)). Noises in two signal detection channels $|Q_1|$ and $|Q_2|$ corresponding to area at the bottom of the image (ROI_1 in Fig. 2(c)) were assumed to be uncorrelated, each experimentally exhibiting in time domain a statistically Gaussian distribution function centered

Biomedical Optics EXPRESS

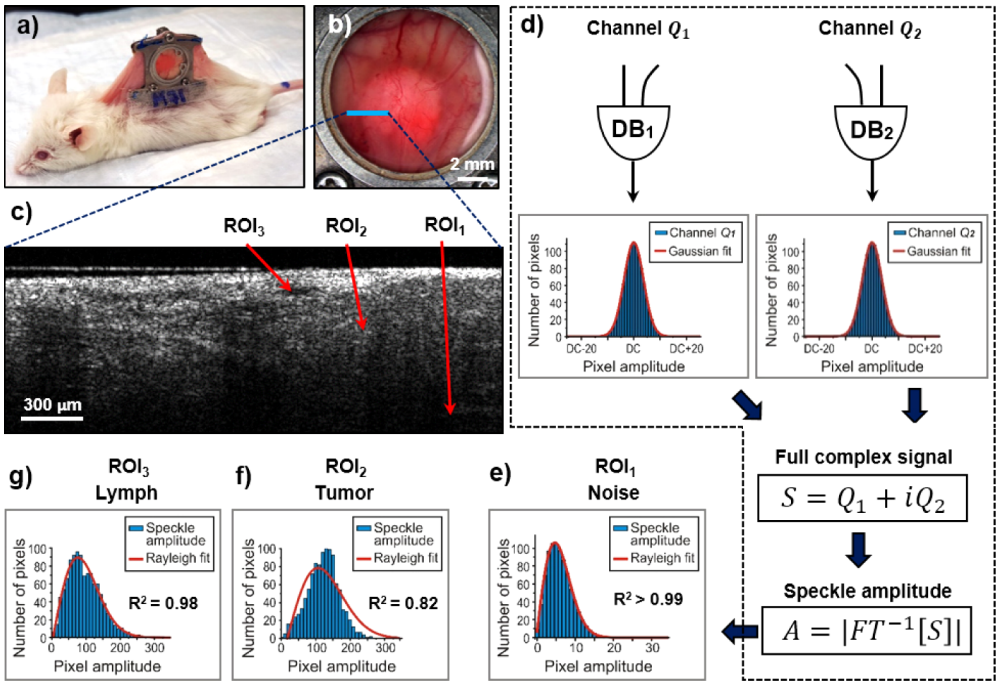

Fig. 2. Speckle statistical data analysis of OCT images. **(a)** White-light photo of a mouse with installed dorsal skin window chamber; **(b)** The photo of the chamber with grown pancreatic adenocarcinoma tumor. Blue line indicates the location of **(c)** the structural OCT image. ROI_1 – deep location (noise area), ROI_2 - solid tumor tissue, ROI_3 - lymphatic vessel lumen; **(d)** Speckle statistics for OCT signal noise: left and right are statistics for detection channels $|Q_1|$ and $|Q_2|$ used to form full complex signal S. DB – dual balanced photo-detector (for details see Fig. 1); **(e)** Speckle statistics of the noise speckle amplitudes A in ROI_1, well described by the Rayleigh distribution ($R^2 = 0.9996$); **(f)** Speckle statistics of the signal-rich tumor tissue in ROI_2, displaying a poorer Rayleigh fit ($R^2 = 0.82$); **(g)** Speckle statistics of the lymphatic vessel lumen in ROI_3, showing closer-to-noise goodness of fit ($R^2 = 0.98$). Red curves correspond to Gaussian fit for (d), and Rayleigh fit for (e), (f) and (g).

on the DC component (red curve, Fig. 2(d); $R^2 > 0.999$). After DC component subtraction and inverse Fourier transform of the complex spectral amplitude $S = Q_1 + iQ_2$,

$$A = |FT^{-1}[S]|, \tag{2}$$

the resulting statistical distribution of the noise speckle amplitudes A in ROI_1 is very well described by the three-parameter Rayleigh distribution function [40]:

$$P(x; a, b, c) = \frac{a(x-c)}{b^2} e^{\frac{-(x-c)^2}{2b^2}}, \tag{3}$$

where a is the amplitude normalization parameter, b - power distribution function parameter and c - shifting parameter (red curve, Fig. 2(e); $R^2 > 0.99$).

As was shown in a number of publications including Refs. [35,36], as well as in our earlier controlled phantom studies [41], with the increasing number of identical scatterers per coherence volume, the corresponding speckle statistics will asymptotically lead to a Rayleigh distribution. However, while applicable to a homogenous medium with identical and discrete

Biomedical Optics EXPRESS

random-particulate scatterers, this argument is only loosely applicable to biological tissues, a medium with a fundamentally different nature (inhomogenous medium with random-continua scatterers). Speckle amplitude statistics for solid tissue signals (tumor in ROI_2) differ from ROI_1 noise signals as demonstrated in Fig. 2(f). For such signal-rich areas of imaged tissue, the Rayleigh fit of Eq. (2) does not describe the data well ($R^2 \sim 0.82$, and the shift parameter is two orders of magnitude greater ($c_{tumor} = 17.7$ *vs* $c_{noise} = -0.18$)). Importantly, there is an intermediate fitting regime that forms the basis of the proposed methodology: for lymphatic vessel lumen signal from ROI_3 as demonstrated in Fig. 2(g), the speckle statistics are close to Rayleigh distribution of noise ($R^2 = 0.984$, as are the individual fit parameters ($c_{lymph} = -0.11$ *vs* $c_{noise} = -0.18$)). We can thus select a suitable goodness-of-fit R^2 range to isolate these semi-transparent tissue structures from noise and from surrounding tissue signals, as described below.

It is important to note here, that although the number of 1080 pixels per ROI was considered to be sufficient to detect structures of interest, these 1080 statistical samples of the speckle distribution per small analysis volume may not be fully independent at OCT's frame rate of 40 Hz and the resultant inter-frame temporal spacing of 25 ms. In our earlier *in-vivo* experiments [42,43] we explored the range of OCT signal decorrelation times for blood, tumor and normal tissues. For blood, decorrelation times were found to range from ~20 ms (0.5 mm/s flow rate in small vessels like capillaries) to ~1 ms (>12 mm/s flow rate in larger vessels); tumor and normal tissues had much longer decorrelation times reaching ~500 ms and 1.1s (skin), respectively. Decorrelation times for lymphatics have not been measured, but assuming similarity with slow blood flow, these may be roughly estimated to be several to tens of milliseconds. Therefore, at inter-frame temporal spacing of 25 ms, the signals from "liquid" voxels (blood, lymphatics) are largely decorrelated, whereas those from "solid" regions likely remain significantly correlated. This may cause some deviations from fully developed signal histogram distributions (e.g., Fig. 2(f)) and their goodness-of-fit R^2 by Rayleigh distribution of noise.

Optimal inter-frame times and number of repeat B-scans are also yet to be determined. Further, M-mode-like acquisition patterns developed for blood microangiography [44] may prove beneficial for this application, whereby rapidly acquired high-density B-scans with hundreds of A-scans in a resolution volume will still allow the formation of speckle statistics in noise regions commensurate with the described Rayleigh fitting procedure.

2.4. Microvasculature (blood and lymph) and nerves detection

We utilize the statistical distribution functions of complex signal speckle amplitudes, specifically their similarity to the Rayleigh fit indicative on pure noise, to separate out lymphatic vessels and nerves from OCT images as shown schematically in Fig. 3. Figure 3(a) shows the white light photo of a pancreatic adenocarcinoma tumor grown in a window chamber model (6×6 mm^2 field of view). Recorded 24 B-scans (Fig. 3(b)) at each lateral location are used for simultaneous mapping of low-scattering tissues by newly proposed speckle filtering method (left side) and microvascular angiographic imaging (right side). As shown on the left in Fig. 3(c), nerves and lymphatic vessels mapping consists of two simple steps. First, speckle amplitudes from each voxel are plotted as a histogram and fitted with Rayleigh distribution function to find the R^2 value. Secondly, empirically chosen $0.95 < R^2 < 0.99$ thresholding range is applied to the entire volumetric image to map nerves and lymphatic vessels in 3D; these are then superimposed in cyan color on the same B-scan (shown in lateral view average intensity projection below it). Note that nerves appear as oval-shaped structures surrounded by optically semi-transparent tissue; this identification is confirmed by multi-stain histology, as described below (see Results and Discussion). Further, the above R^2 threshold range choice is not unique nor selected from theoretical considerations; this is simply an empirical first-pass discrimination for the purposes of this proof-of-principle demonstrations based on the analysis summarized in Fig. 2. Improved thresholding selections, including the possible use a-b-c fitting parameter space as per Eq. (3) to

Biomedical Optics EXPRESS

supplement the R^2 metric, will be pursued in future studies as briefly mentioned in the Results and Discussion section.

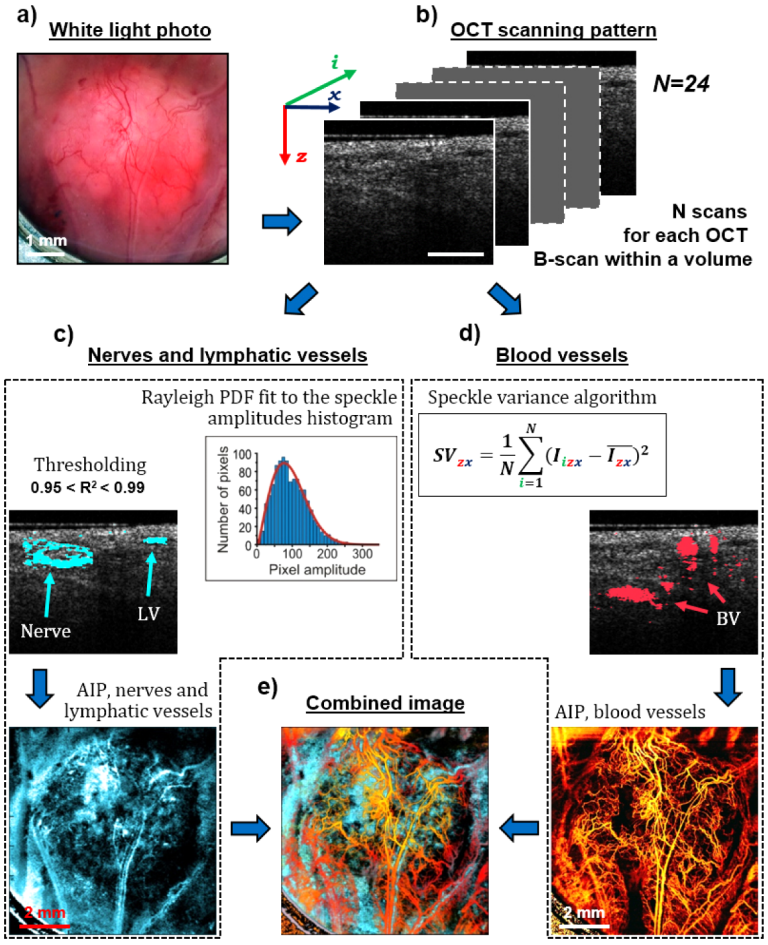

Fig. 3. Simultaneous mapping of low-scattering tissues by spatial speckle filtering and of blood vessels by temporal speckle variance methods. **(a)** The white light photo of a pancreatic adenocarcinoma tumor grown in a window chamber model; **(b)** $N = 24$ OCT B-scans from the same lateral location within the scanned volume. Scale bar is 0.3 mm; **(c)** Nerves and lymphatic vessels mapping. *Step 1*: Speckle amplitudes from each voxel are plotted as a histogram and fitted with Rayleigh distribution function to find the R^2 value. *Step 2*: $0.95 < R^2 < 0.99$ thresholding is applied to the entire imaged volume to map nerves and lymphatic vessels (shown in the same B-scan as in (b), and in a lateral-view average intensity projection (AIP) below it). Nerves appear as oval ring-shaped structures. LV-lymphatic vessel; **(d)** Blood vessels mapping using conventional speckle variance algorithm (shown in the same B-scan as in (b) and in average intensity projection (AIP) below it). BV – blood vessel; **(e)** Combined 3D volumes of lymphatic/blood vessels and nerves, presented in a lateral-view average intensity projection form.

The right side of the figure (Fig. 3(d)) shows the OCT blood angiography as performed using conventional speckle variance algorithm [35]; this is displayed on the same B-scan and in lateral view average intensity projection below it. The resultant bottom left (lymphatics and nerves) and bottom right (blood microvasculature) are inherently co-registered; the final step would be to combine both 3D volumes, as presented in Fig. 3(e) in a lateral view average intensity projection

Biomedical Optics EXPRESS

form. To do this properly in 3D, however, so as to furnish additional helpful visual information will require more research; this will also be pursued in future studies and be reported in a separate publication. For the remainder of this work we thus display the lymphatics/nerves and blood angiograms separately: blood microvasculature depth-encoded in RGB color space as described previously (green-yellow-red-grey shallow to deep color map) [45] and lymphatics/nerves in a grey-scale color map.

3. Results and discussion

3.1. Normal skin

Microarchitecture of healthy vascular network is known to be hierarchically organized with ordered and evenly distributed blood vessels to allow adequate perfusion of nutrients and oxygen to all cells [46]. Indeed, both white-light microphotography (Fig. 4(a)) and speckle-variance OCT

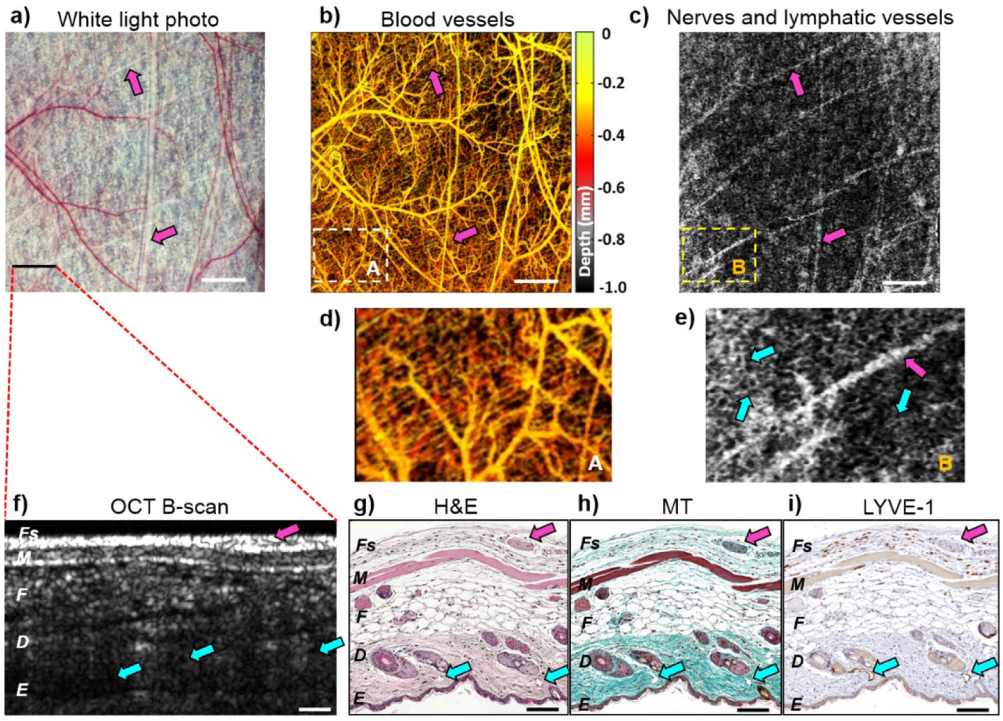

Fig. 4. Mouse dorsal skin angiography, lymphangiography/neurography, and histology. **(a)** White-light photo of dorsal skin in window chamber, field of view = 6×6 mm^2. **(b)** Depth-encoded blood microvasculature map of (a). **(c)** Grey-scale average R^2– thresholded projection for low-scattering regions in (a). Dashed-line white (**A**) and yellow (**B**) rectangular areas are expanded in **(d)** for blood microvasculature, and **(e)** for lymphatic vessels and nerves, some of which are labeled with arrows, the former as cyan and the latter as purple. **(f)** OCT B-scan with histological stains in (g), (h) and (i) from approximately same location in tissue. **(g)** Overall tissue architecture and cellular morphology are visualized with Hematoxylin and Eosin (H&E) staining; **(h)** Nerves are distinguished from surrounding connective tissues with Masson's Trichrome (MT) staining; **(f)** Lymphatic vessels are visualized with lymphatic vessel endothelial hyaluronan receptor 1 (LYVE-1). Tissue layers are labelled in the bottom row images as Fs – fascia, M- muscle, F – fat, D – dermis, E – epidermis. Nerves are labeled with purple arrows, lymphatic vessels – with cyan arrows. Scale bars in top row panels are 1 mm; in bottom row are 0.1 mm.

Biomedical Optics EXPRESS

(Fig. 4(b), shown in a color depth-encoded view) of normal skin blood network clearly demonstrate this. Faint lightly colored vessel-like structures are seen in the white light photomicrograph, perhaps indicative of lymph vessels or nerves; these faint "lines" are not visible in the svOCT blood angiograph. The speckle analysis and threshold filtering method described in this paper now allows detailed visualization of these semi-transparent structures, as shown in Fig. 4(c); the detected lymphatic / nerve networks also appear highly organized with regular coverage of the whole area. To determine which one is which was not possible from white light and OCT images alone, and required detailed histological correlative validation studies as presented in the bottom row panels of Fig. 4.

Figure 4(f) shows a representative OCT cross-sectional structural B-mode scan from the imaged normal skin region, along with three histological sections stained with H&E, Masson's Trichrome, and LYVE-1 (Fig. 4(g-i)). From the detailed comparison of locations, shapes, and compositions of the various tissue components seen on multi-stain histology with the OCT (and white light) images, we were able to identify the visualized structures of Fig. 4c. Specifically, the tree-like structures are the lymphatic vessels located primarily close to the epidermis that stain with lymph-vessel-specific LYVE-1 (cyan arrows on Fig. 4(i)). Conversely, the more straight runs seen on *en-face* views of the top row images are nerves located in the fascia, as clearly revealed in Masson's Trichrome histology (purple arrows on Fig. 4(h), highlighting the connective tissue sheath that typically surrounds a nerve fascicle; note that these structures do not stain with LYVE-1, so cannot be lymphatic vessels). Armed with this interpretation from multi-stain histology, we labeled the OCT-predicted regions ($0.95 < R^2 < 0.99$ similarity to the Rayleigh distribution) with purple arrows to indicate nerves on all panels of Fig. 4, and likewise labeled lymphatics with cyan. Going back to the OCT maps of Figs. 4(b) and 4(c), the white (A) and yellow (B) rectangle regions from the same locations are shown zoomed in below for comparison (Figs. 4(d) - blood vessels and 4(e) - nerves and lymphatics). In the Fig. 4e we have likewise labeled some of the OCT-detected nerves and lymphatics with purple and cyan arrows, respectively. As seen, the nerve and lymphatic structures of normal mouse skin also show a relatively regular and ordered pattern, in analogy with the visualized blood network in Fig. 4(d).

3.2. Tumor

Moving on from normal to pathologic imaging, Fig. 5 shows considerably different patterns when pancreatic adenocarcinoma is examined. Rapidly growing tumor mass infiltrates surrounding normal tissues and changes their anatomy. The white light photomicrograph of Fig. 5(a) shows increase swelling and redness; this is borne out by the extensive, highly vascularized but more chaotic microvascular network seen in Fig. 5(b). Lymphatic vessels and nerves detected in Fig. 5(c) also appear somewhat enlarged and chaotic compared to normal tissue architecture. The zoomed-in views of Figs. 5(d) and 5(e), where the two areas (A and B) have been enlarged as per Fig. 4, indeed show disorganized labyrinth of blood vessels (A) and thicker lymphatics (B). In analogy with the normal tissue analysis of Fig. 4, the bottom row panels show an OCT cross-sectional scan (Fig. 5(f)) from the region near the tumour edge indicated on Fig. 5(a) along with histological validation using three different stains (Fig. 5(g-i)). Compared to normal tissues, this tumour edge region reveals the lack of distinct tissue layers seen on histology, thicker nerves (purple arrows) and lymphatic vessels (cyan arrows). In contrast to the edges, the core of the tumor seen in Fig. 5(c) presents the tangled circuitry of immature lymphatic vessels of larger diameters. LYVE-1 staining in Fig. 5(j) corresponding to the green line in the threshold-filtered OCT map of Fig. 5(c), clearly identifies two newly formed lymphatic vessels with thinner walls. These appear filled and are most likely not functional, as previously reported using ferritin-positive tracking and molecular lymphatic marker Prox-1 immunostaining [47].

Biomedical Optics EXPRESS

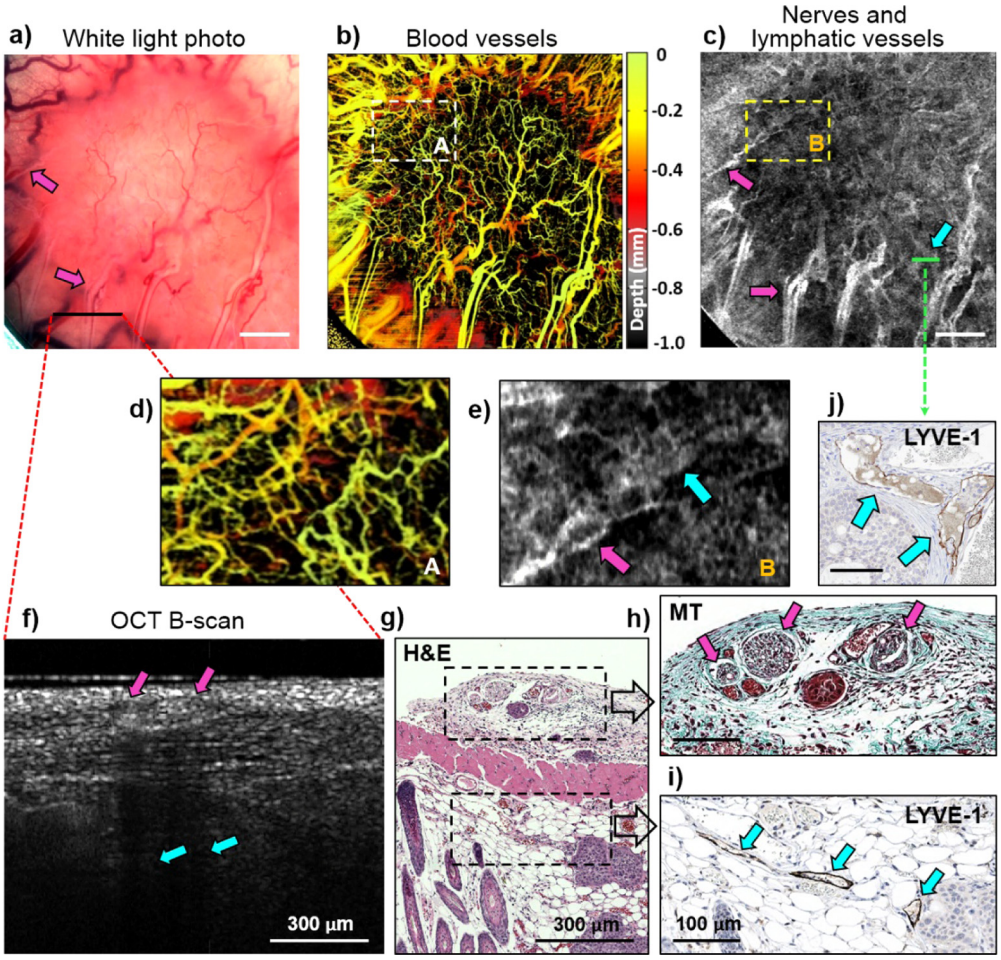

Fig. 5. Angiography, lymphangiography/neurography and histology of pancreatic adenocarcinoma grown in a mouse dorsal skin window chamber. **(a)** White-light photo of dorsal skin in window chamber, field of view – 6×6 mm^2; **(b)** Depth-encoded blood microvasculature map of (a); **(c)** Grey-scale average R^2– thresholded projection for low-scattering regions in (a). Dashed-line white (**A**) and yellow (**B**) rectangular areas are expanded in **(d)** for blood microvasculature, and **(e)** for lymphatic vessels and nerves, some of which are labeled with arrows, the former as cyan and the latter as purple. Scale bars in (a), (b) and (c) are 1 mm; **(f)** OCT B-scan with corresponding Hematoxylin and Eosin (H&E) staining in **(g)** from approximately same location in tissue. Black dash-lined rectangular areas are enlarged in (g) and (h); **(h)** Nerves are distinguished from surrounding connective tissues with Masson's Trichrome (MT) staining; **(i)** Peri-tumoral lymphatic vessels are visualized with lymphatic vessel endothelial hyaluronan receptor 1 (LYVE-1). Nerves are labeled with purple arrows, lymphatic vessels – with cyan arrows. **(j)** LYVE-1 staining of the tumor core tissue (location labeled with green line in (c)), identifying two newly formed lymphatic vessels with thinner walls. Scale bars in (h), (i) and (j) are 0.1 mm.

Figures 4 and 5 demonstrate the main advantage of the new method – controlled detection of tissues of interest without operator dependence. Indeed, accurate selection of lymphatics-containing tissue layers, one of the main challenges in negative-contrast approaches, is not an issue with the proposed speckle filtering methodology. Further, destructive interference challenge

Biomedical Optics EXPRESS

causing low-signal artefacts, OCT imager-specific depth attenuation compensation, lymphatics vesselness filtering and other complex and computationally expensive procedures discussed in the Introduction become unnecessary. Instead, a direct 2-step process is employed involving (1) Rayleigh fit to speckle amplitudes histogram and (2) R^2 goodness-of-fit metric thresholding.

A direct consequence of the quality of the proposed methodology is the demonstrated detection of the neural network. To the best of our knowledge, this is the first *in-vivo* OCT nerve visualization in normal and tumor tissues outside of ophthalmology, opening the door to many exciting applications in local anesthesia administration and neurosurgical avoidance of enervated tissue regions. However, to explore these properly, further methodology improvements are needed to distinguish between the visualized lymphatics and nerves. These technique refinements will develop models for non-empirical thresholds selection, explore the information contained in the three-parameter space of the Rayleigh fit, and find appropriate ways to combine the blood, lymph and neural networks in three-dimensional volumetric composite images for enhanced visualization and quantification.

Overall, the reported speckle statistics difference between lymph/nerves and pure noise may be partly due to tissue heterogeneity versus noise homogeneity effects (within the ROIs selected for analysis). To address this, we have recently started to simulate the OCT speckle patterns using the approach described in Refs. [48,49] for zero-to-low scatterer concentrations and effects of varying ROI sizes; the outcomes of this research will be reported in a separate publication.

4. Conclusion

In conclusion, we have presented a new OCT method for simultaneous *in-vivo* detection of nerves and lymphatic vessels. In comparison with previous negative-contrast techniques, it does not require signal attenuation evaluation and compensation, and addresses OCT speckle destructive interference issues. At low-scattering OCT signal levels approaching the system noise floor, the proposed method distinguishes tissue nerve and lymph optical signatures using speckle statistical parameters. To the best of our knowledge, direct nerves detection by OCT has not been reported outside of ophthalmology; this may have exciting applications including image-guided local anesthetics injection into nerve-containing tissues in interventional procedure, or accurate removal of pathological tissue with minimal disruption of surrounding neuronal matter in neurosurgery. Future work will attempt to separate lymphatic vessels from nerves by improved R^2 metric thresholding selection, closer examination of the a-b-c Rayleigh fitting parameter space (Eq. (3)) and furnishing additional visual / quantifiable information by combining blood, lymph and neural networks into composite three-dimensional images.

Funding

Canadian Institutes of Health Research (CIHR) (173971); Terry Fox Foundation (STARS21 Program); Russian Foundation for Basic Research (RFBR) (19-02-00645); Council on grants of the President of the Russian Federation (МК-3416.2018.2).

Acknowledgments

The authors thank Dr. Trevor McKee and Mr. Napoleon Law for their assistance in histological evaluation of tissue samples for this study. The OCT system was developed at the National Research Council of Canada with contribution from Drs. Linda Mao, Shoude Chang, Sherif Sherif, and Erroll Murdock.

Disclosures

The authors declare that there are no conflicts of interest related to this article.

Biomedical Optics EXPRESS

References

1. B. J. Vakoc, R. M. Lanning, J. A. Tyrrell, T. P. Padera, L. A. Bartlett, T. Stylianopoulos, L. L. Munn, G. J. Tearney, D. Fukumura, R. K. Jain, and B. E. Bouma, "Three-dimensional microscopy of the tumor microenvironment *in vivo* using optical frequency domain imaging," Nat. Med. **15**(10), 1219–1223 (2009).
2. K. Alitalo, "The lymphatic vasculature in disease," Nat. Med. **17**(11), 1371–1380 (2011).
3. S. A. Stacker, S. P. Williams, T. Karnezis, R. Shayan, S. B. Fox, and M. G. Achen, "Lymphangiogenesis and lymphatic vessel remodelling in cancer," Nat. Rev. Cancer **14**(3), 159–172 (2014).
4. O. Birim, A. P. Kappetein, T. Stijnen, and A. J. Bogers, "Meta-analysis of positron emission tomographic and computed tomographic imaging in detecting mediastinal lymph node metastases in nonsmall cell lung cancer," Ann. Thorac. Surg. **79**(1), 375–382 (2005).
5. Q. Lu, J. Hua, M. M. Kassir, Z. Delproposto, Y. Dai, J. Sun, M. Haacke, and J. Hu, "Imaging lymphatic system in breast cancer patients with magnetic resonance lymphangiography," PLoS One **8**(7), e69701 (2013).
6. E. Sevick, R. Sharma, J. Rasmussen, M. Marshall, J. Wendt, H. Q. Pham, E. Bonefas, J. P. Houston, L. Sampath, K. E. Adams, D. Blanchard, R. Fisher, S. B. Chiang, R. Elledge, and M. Mawad, "Imaging of lymph flow in breast cancer patients after microdose administration of a near-infrared fluorophore: feasibility study1," Radiology **246**(3), 734–741 (2008).
7. K. Yasufuku, T. Nakajima, K. Motoori, Y. Sekine, K. Shibuya, K. Hiroshima, and T. Fujisawa, "Comparison of endobronchial ultrasound, positron emission tomography, and CT for lymph node staging of lung cancer," Chest **130**(3), 710–718 (2006).
8. K. Hayashi, P. Jiang, K. Yamauchi, N. Yamamoto, H. Tsuchiya, K. Tomita, A. R. Moossa, M. Bouvet, and R. M. Hoffman, "Real-time imaging of tumor-cell shedding and trafficking in lymphatic channels," Cancer Res. **67**(17), 8223–8228 (2007).
9. D. P. Popescu, L. P. Choo-Smith, C. Flueraru, Y. Mao, S. Chang, J. Disano, S. Sherif, and M. G. Sowa, "Optical coherence tomography: fundamental principles, instrumental designs and biomedical applications," Biophys. Rev. **3**(3), 155–169 (2011).
10. V. Demidov, A. Maeda, M. Sugita, V. Madge, S. Sadanand, C. Flueraru, and I. A. Vitkin, "Preclinical longitudinal imaging of tumor microvascular radiobiological response with functional optical coherence tomography," Sci. Rep. **8**(1), 38 (2018).
11. P. Gong, S. Es'haghian, K. A. Harms, A. Murray, S. Rea, F. M. Wood, D. D. Sampson, and R. A. McLaughlin, "In vivo label-free lymphangiography of cutaneous lymphatic vessels in human burn scars using optical coherence tomography," Biomed. Opt. Express **7**(12), 4886–4898 (2016).
12. S. Yousefi, J. Qin, Z. Zhi, and R. K. Wang, "Label-free optical lymphangiography: development of an automatic segmentation method applied to optical coherence tomography to visualize lymphatic vessels using Hessian filters," J. Biomed. Opt. **18**(8), 086004 (2013).
13. M. Almasian, N. Bosschaart, T. G. van Leeuwen, and D. J. Faber, "Validation of quantitative attenuation and backscattering coefficient measurements by optical coherence tomography in the concentration- dependent and multiple scattering regime," J. Biomed. Opt. **20**(12), 121314 (2015).
14. P. Gong, D. Y. Yu, Q. Wang, P. K. Yu, K. Karnowski, M. Heisler, A. Francke, D. An, M. V. Sarunic, and D. D. Sampson, "Label-free volumetric imaging of conjunctival collecting lymphatics ex vivo by optical coherence tomography lymphangiography," J. Biophotonics **11**(8), e201800070 (2018).
15. G. N. Armaiz-Pena, S. K. Lutgendorf, S. W. Cole, and A. K. Sood, "Neuroendocrine modulation of cancer progression," Brain, Behav., Immun. **23**(1), 10–15 (2009).
16. F. Y. Feng, Y. Qian, M. H. Stenmark, S. Halverson, K. Blas, S. Vance, H. M. Sandler, and D. A. Hamstra, "Perineural invasion predicts increased recurrence, metastasis, and death from prostate cancer following treatment with dose-escalated radiation therapy," Int. J. Radiat. Oncol., Biol., Phys. **81**(4), e361–e367 (2011).
17. S. Li, Y. Sun, and D. Gao, "Role of the nervous system in cancer metastasis," Oncol. Lett. **5**(4), 1101–1111 (2013).
18. P. Seifert and M. Spitznas, "Tumours may be innervated," Virchows Arch. **438**(3), 228–231 (2001).
19. D. Albo, C. L. Akay, C. L. Marshall, J. A. Wilks, G. Verstovsek, H. Liu, N. Agarwal, D. H. Berger, and G. E. Ayala, "Neurogenesis in colorectal cancer is a marker of aggressive tumor behavior and poor outcomes," Cancer **117**(21), 4834–4845 (2011).
20. J. H. Li, Q. Y. Ma, S. G. Shen, and H. T. Hu, "Stimulation of dorsal root ganglion neurons activity by pancreatic cancer cell lines," Cell Biol. Int. **32**(12), 1530–1535 (2008).
21. F. Entschladen, D. Palm, B. Niggemann, and K. S. Zaenker, "The cancer's nervous tooth: considering the neuronal crosstalk within tumors," Semin. Cancer Biol. **18**(3), 171–175 (2008).
22. M. Khasraw and J. B. Posner, "Neurological complications of systemic cancer," Lancet Neurol. **9**(12), 1214–1227 (2010).
23. M. Jhawer, D. Coit, M. Brennan, L. X. Qin, M. Gonen, D. Klimstra, L. Tang, D. P. Kelsen, and M. A. Shah, "Perineural invasion after preoperative chemotherapy predicts poor survival in patients with locally advanced gastric cancer: gene expression analysis with pathologic validation," Am. J. Clin. Oncol. **32**(4), 356–362 (2009).
24. M. E. Miller, B. Palla, Q. Chen, D. A. Elashoff, E. Abemayor, J. M. St. John, and C. K. Lai, "A novel classification system for perineural invasion in noncutaneous head and neck squamous cell carcinoma: histologic subcategories and patient outcomes," Am. J. Otolaryngol. **33**(2), 212–215 (2012).

Biomedical Optics EXPRESS

25. A. Filler, "MR neurography and diffusion tensor imaging: origins, history & clinical impact," Neurosurgery **65**(suppl_4), A29–A43 (2009).
26. S. K. Thawait, V. Chaudhry, G. K. Thawait, K. C. Wang, A. Belzberg, J. A. Carrino, and A. Chhabra, "High-resolution MR neurography of diffuse peripheral nerve lesions," Am. J. Neuroradiol. **32**(8), 1365–1372 (2011).
27. L. M. Sakata, J. Deleon-Ortega, V. Sakata, and C. A. Girkin, "Optical coherence tomography of the retina and optic nerve - a review," Clin. Experiment. Ophthalmol. **37**(1), 90–99 (2009).
28. C. Lamirel, N. J. Newman, and V. Biousse, "Optical coherence tomography (OCT) in optic neuritis and multiple sclerosis," Rev. Neurol. **166**(12), 978–986 (2010).
29. G. A. Dumanian, M. A. McClinton, and T. M. Brushart, "The effects of free fat grafts on the stiffness of the rat sciatic nerve and perineural scar," J. Hand Surg. **24**(1), 30–36 (1999).
30. J. Hope, B. Braeuer, S. Amirapu, A. McDaid, and F. Vanholsbeeck, "Extracting morphometric information from rat sciatic nerve using optical coherence tomography," J. Biomed. Opt. **23**(11), 1 (2018).
31. C. A. Chlebicki, A. D. Lee, W. Jung, H. Li, L. H. Liaw, Z. Chen, and B. J. Wong, "Preliminary investigation on use of high-resolution optical coherence tomography to monitor injury and repair in the rat sciatic nerve," Lasers Surg. Med. **42**(4), 306–312 (2010).
32. D. T. Raphael, C. Yang, N. Tresser, J. Wu, Y. Zhang, and L. Rever, "Images of spinal nerves and adjacent structures with optical coherence tomography: preliminary animal studies," J. Pain **8**(10), 767–773 (2007).
33. F. P. Henry, Y. Wang, C. Rodriguez, M. A. Randolph, E. Rust, J. M. Winograd, J. F. de Boer, and B. H. Park, "In vivo optical microscopy of peripheral nerve myelination with polarization sensitive-optical coherence tomography," J. Biomed. Opt. **20**(4), 046002 (2015).
34. J. M. Schmitt, S. H. Xiang, and K. M. Yung, "Speckle in optical coherence tomography," J. Biomed. Opt. **4**(1), 95 (1999).
35. A. Mariampillai, B. A. Standish, E. H. Moriyama, M. Khurana, N. R. Munce, M. K. Leung, J. Jiang, A. Cable, B. C. Wilson, I. A. Vitkin, and V. X. Yang, "Speckle variance detection of microvasculature using swept-source optical coherence tomography," Opt. Lett. **33**(13), 1530–1532 (2008).
36. M. Almasian, T. G. van Leeuwen, and D. J. Faber, "OCT amplitude and speckle statistics of discrete random media," Sci. Rep. **7**(1), 14873–11 (2017).
37. Y. Mao, S. Sherif, C. Flueraru, and S. Chang, "3×3 Mach-Zehnder interferometer with unbalanced differential detection for full-range swept-source optical coherence tomography," Appl. Opt. **47**(12), 2004–2010 (2008).
38. Y. Mao, C. Flueraru, S. Chang, D. Popescu, and M. Sowa, "High-quality tissue imaging using a catheter-based swept-source optical coherence tomography systems with an integrated semiconductor optical amplifier," IEEE Trans. Instrum. Meas. **60**(10), 3376–3383 (2011).
39. R. K. Wang, "Directional blood flow imaging in volumetric optical microangiography achieved by digital frequency modulation," Opt. Lett. **33**(16), 1878–1880 (2008).
40. B. Karamata, K. Hassler, M. Laubscher, and T. Lasser, "Speckle statistics in optical coherence tomography," J. Opt. Soc. Am. A **22**(4), 593–596 (2005).
41. A. Weatherbee, M. Sugita, K. Bizheva, I. Popov, and A. Vitkin, "Probability density function formalism for optical coherence tomography signal analysis: a controlled phantom study," Opt. Lett. **41**(12), 2727–2730 (2016).
42. H. Assadi, V. Demidov, R. Karshafian, A. Douplik, and A. Vitkin, "Microvascular contrast enhancement in optical coherence tomography using microbubbles," J. Biomed. Opt. **21**(7), 076014 (2016).
43. V. Demidov, O. Demidova, A. Shabunin, and A. Vitkin, "Alternative contrast mechanism in optical coherence tomography: temporal speckle synchronization effects," Modern Tech. Med. **10**(1), 39–48 (2018).
44. L. A. Matveev, V. Y. Zaitsev, G. V. Gelikonov, A. L. Matveyev, A. A. Moiseev, S. Y. Ksenofontov, V. M. Gelikonov, M. A. Sirotkina, N. D. Gladkova, V. Demidov, and A. Vitkin, "Hybrid M-mode-like OCT imaging of three-dimensional microvasculature in vivo using reference-free processing of complex valued B-scans," Opt. Lett. **40**(7), 1472–1475 (2015).
45. V. Demidov, X. Zhao, O. Demidova, H. Y. M. Pang, C. Flueraru, F. F. Liu, and I. A. Vitkin, "Preclinical quantitative *in-vivo* assessment of skin tissue vascularity in radiation induced fibrosis with optical coherence tomography," J. Biomed. Opt. **23**(10), 1 (2018).
46. R. K. Jain, "Delivery of novel therapeutic agents in tumors: physiological barriers and strategies," J. Natl. Cancer Inst. **81**(8), 570–576 (1990).
47. N. Isaka, T. P. Padera, J. Hagendoorn, D. Fukumura, and R. K. Jain, "Peritumor lymphatics induced by Vascular Endothelial Growth Factor-C exhibit abnormal function," Cancer Res. **64**(13), 4400–4404 (2004).
48. V. Y. Zaitsev, L. A. Matveev, A. L. Matveyev, G. V. Gelikonov, and V. M. Gelikonov, "A model for simulating speckle-pattern evolution based on close to reality procedures used in spectral-domain OCT," Laser Phys. Lett. **11**(10), 105601 (2014).
49. A. L. Matveyev, L. A. Matveev, A. A. Moiseev, A. A. Sovetsky, G. V. Gelikonov, and V. Y. Zaitsev, "Semi-analytical full-wave model for simulations of scans in optical coherence tomography with accounting for beam focusing and the motion of scatterers," Laser Phys. Lett. **16**(8), 085601 (2019).